



HAL
open science

Hydride-Containing Eight-Electron Pt/Ag Superatoms: Structure, Bonding, and Multi-NMR Studies

Tzu-Hao Chiu, Jian-Hong Liao, Franck Gam, Ying-Yann Wu, Xiaoping Wang,
Samia Kahlal, Jean-Yves Saillard, C W Liu

► **To cite this version:**

Tzu-Hao Chiu, Jian-Hong Liao, Franck Gam, Ying-Yann Wu, Xiaoping Wang, et al.. Hydride-Containing Eight-Electron Pt/Ag Superatoms: Structure, Bonding, and Multi-NMR Studies. *Journal of the American Chemical Society*, 2022, 144 (23), pp.10599-10607. 10.1021/jacs.2c03715 . hal-03715367

HAL Id: hal-03715367

<https://hal.science/hal-03715367>

Submitted on 11 May 2023

HAL is a multi-disciplinary open access archive for the deposit and dissemination of scientific research documents, whether they are published or not. The documents may come from teaching and research institutions in France or abroad, or from public or private research centers.

L'archive ouverte pluridisciplinaire **HAL**, est destinée au dépôt et à la diffusion de documents scientifiques de niveau recherche, publiés ou non, émanant des établissements d'enseignement et de recherche français ou étrangers, des laboratoires publics ou privés.

Hydride-containing 8-electron Pt/Ag Superatoms: Structure, Bonding and Multi-NMR Studies

Tzu-Hao Chiu,^a Jian-Hong Liao,^a Franck Gam,^d Ying-Yann Wu,^b Xiaoping Wang,^c Samia Kahlal,^d Jean-Yves Saillard,^{d*} and C. W. Liu^{a*}

^a Department of Chemistry, National Dong Hwa University, Hualien 974301, Taiwan (Republic of China)

^b Institute of Chemistry, Academia Sinica, Taipei 11528, Taiwan (Republic of China)

^c Neutron Scattering Division, Neutron Sciences Directorate, Oak Ridge National Laboratory, Oak Ridge, TN 37831, U.S.A.

^d Univ Rennes, CNRS, ISCR-UMR 6226, F-35000 Rennes, France

* Correspondence: E-mail: chenwei@mail.ndhu.edu.tw; Tel: +886-3-890-3607; Fax : +886-3-890-0162; <http://faculty.ndhu.edu.tw/~cwl/index.htm>

Keywords: Platinum, Silver, Hydride, Neutron diffraction, Superatom

Abstract

Recent reports on hydride-doped noble metal nanoclusters (*J. Am. Chem. Soc.* **2018**, *140*, 12314; *Angew. Chem. Int. Ed.* **2021**, *60*, 22293) strongly suggest that the encapsulated hydride is a part of *superatom* core, but no accurate location of the hydride could be experimentally proved, so far. We report herein a hydride-doped 8-electron platinum/silver alloy nanocluster in which the position of four-coordinated hydride was determined by neutron diffraction for the first time. X-ray structures of [PtHAg₁₉(dtp/desp)₁₂] (dtp = S₂P(OⁿPr)₂ (**1**); dsep = Se₂P(OⁱPr)₂ (**2**)) describe a central platinum hydride (PtH) unit encapsulated within a distorted Ag₁₂ icosahedron, the resulting (PtH)@Ag₁₂ core being stabilized by an outer sphere made up of seven capping silver atoms and twelve dichalcogenolates. Solid-state structures of **1** and **2**

differ somewhat in the spatial configuration of their outer spheres, resulting in overall different symmetries, C_1 and C_3 , respectively. Whereas the multi-NMR spectra of **2** in solution at 173K reveal that the structure of C_3 symmetry is the predominant one, ^1H and ^{195}Pt NMR spectra of **1** at the same temperature disclose the presence of isomers of both C_1 and C_3 symmetry. DFT calculations found both isomers to be very close in energy, supporting the fact that they co-exist in solution. They also show that the $[\text{PtH@Ag}_{12}]^{5+}$ kernel can be viewed as a closed-shell *superatomic* core, the μ_4 -hydride electron contributing to its 8-electron count. On the other hand, the 1s(H) orbital contributes only moderately to the *superatomic* orbitals, being mainly involved in the building of a Pt-H bonding electron pair with the $5d_z^2(\text{Pt})$ orbital. The two compounds display differences in photoluminescence, compound **2** exhibiting a strong phosphorescence emission at 77K.

Introduction

Researches on alloy nanoclusters (NCs) have become topical because of the presence of unique stability and distinct catalytic activities compared with homometallic counterparts.¹⁻⁶ In general these atomically precise NCs are protected by monothiols, dithiols, carbenes, tertiary phosphines, halogens, etc. In recent years, a class of nanoscale metal-hydride species has gradually expanded from copper-rich clusters to gold- or silver-rich clusters.⁷⁻¹⁵ However, most of these clusters (except copper hydrides) are metastable products and they have been extremely challenging in the characterization of hydride positions. As the smallest ligand, H⁻ inclines to occupy positions situated inside the metal core, leading to deformation of the metal framework. After stripping the inner hydride by heating, structure changes accompanied with alteration of cluster nuclearity are frequently observed.¹³⁻¹⁸ Hence more researches on metal hydrides are needed to facilitate the understanding of metal nanocluster evolutions, especially for those that were formed *via* reduction routes.

Upon reacting with Lewis acids such as salts of group 11 metals, interstitial hydrides can behave as 2-electron ligands to establish donor-acceptor relationships.¹⁸⁻²⁰ Examples are explicitly demonstrated on the two encapsulated hydrides of [Cu₁₁H₂(dtp)₆(C₂Ph)₃].^{20,21} In addition, an interstitial hydride connected to noble metals, whose electronegativity values are larger than that of H, can behave as a "metallic" hydrogen.⁸⁻¹³ Tsukuda and co-workers reported that the hydride dopant in (HPd@Au₁₀)³⁺ contributes to the cluster 8-electron count, (1S)²(1P)⁶.¹⁰ Sim and Lee put forward to a concept of *superatom-in-superatom*, in which the hydride dopant in [RhH@Ag₂₄(SPhMe₂)₁₈]²⁻ NC provides one electron to the Rh atom, an open d-shell ([Kr]4d⁸5s¹), to form a RhH "superatom" corresponding to a closed shell ([Kr]4d¹⁰).⁸ Unfortunately, the hydride position within these two clusters was only proposed by DFT calculations.^{8,10} Herein, we provide the first structure proof of hydride being a part of

superatom by the synthesis of a new hydride-containing 8-electron alloy cluster, $[\text{PtHAg}_{19}\{\text{S}_2\text{P}(\text{O}^i\text{Pr})_2\}_{12}]$ (**1**), which is fully characterized by ESI-MS spectrometry, UV-vis spectrum, multi-NMR, single crystal X-ray and neutron diffractions. Additionally, a slightly different metal-framework is observed on its Se-analogue, $[\text{PtHAg}_{19}\{\text{Se}_2\text{P}(\text{O}^i\text{Pr})_2\}_{12}]$ (**2**), formed via ligand-exchange induced structure transformation (LEIST) method.^{22, 23} The photoluminescence at 77K is also enhanced after LEIST. To the best of our knowledge, $[\text{PtHAg}_{19}\{\text{S}_2\text{P}(\text{O}^i\text{Pr})_2\}_{12}]$ (**1**) is the first hydride-containing bimetallic superatom certified by neutron diffraction of which the hydride electron participates to the superatomic electron count, $[\text{PtH@Ag}_{12}]^{5+}$, forming an 8-electron species.

Results and discussion

In previous works, we have identified $[\text{M@Ag}_{20}(\text{dtp}/\text{dsep})_{12}]$ ($\text{M} = \text{Pt}$,^{24,25} Pd ,²⁶ dtp and dsep denote dithiophosphate and diselenophosphate, respectively) alloy NCs. They consist of an 8-electron *superatomic* core $[\text{M@Ag}_{12}]^{4+}$ protected by an outer shell made up of 8 peripheral capping Ag^+ and 12 dtp^- or dsep^- dichalcogenolate ligands. The heterometal M is located at the center of an Ag_{12} icosahedron. The alloys passivated by S-donor ligands were synthesized by a one-pot co-reduction method, as exemplified by the formation of $[\text{PtAg}_{20}(\text{dtp})_{12}]$ from the reaction of $[\text{Ag}(\text{CH}_3\text{CN})_4]\text{PF}_6$, $[\text{Pt}\{\text{S}_2\text{P}(\text{O}^i\text{Pr})_2\}_2]$, and $\text{NH}_4[\text{S}_2\text{P}(\text{O}^i\text{Pr})_2]$ followed by the addition of NaBH_4 into the reaction flask. The residual products were separated by column chromatography. In fact, $[\text{PtHAg}_{19}\{\text{S}_2\text{P}(\text{O}^i\text{Pr})_2\}_{12}]$ (**1**) was found in one of the several bands issuing from the same reaction and could be purified, thanks to its polarity different from that of $[\text{PtAg}_{20}\{\text{S}_2\text{P}(\text{O}^i\text{Pr})_2\}_{12}]$. A ligand replacement process was successfully performed by adding 12 equiv. of $\text{NH}_4[\text{Se}_2\text{P}(\text{O}^i\text{Pr})_2]$ into $[\text{PtHAg}_{19}\{\text{S}_2\text{P}(\text{O}^i\text{Pr})_2\}_{12}]$ to yield $[\text{PtHAg}_{19}\{\text{Se}_2\text{P}(\text{O}^i\text{Pr})_2\}_{12}]$ (**2**) within one minute. It is of note that a prolonged stirring

results in decomposition due to the light-sensitive nature of the selenium-donor ligands.

The compositions of **1** and **2** were first determined by positive-mode ESI mass spectrometry. The peak observed at m/z 4911.2669 Da in **Figure 1a** corresponds to the adduct ion $[\mathbf{1} + \text{Ag}^+]^+$ (calc. m/z : 4911.2957 Da). In the spectrum of **2** (**Figure 1b**), the ion peak at m/z 6038.1291 Da corresponds to $[\mathbf{2} + \text{Ag}^+]^+$. (calc. m/z : 6037.9743 Da). Both simulated isotopic patterns match well with their experimental observations.

The X-ray structures of **1** and **2** are depicted in **Figure 2** and selected bond distances and angles are given in **Table 1**. Both metal frameworks of **1** and **2** show a PtH motif encapsulated in a distorted Ag_{12} icosahedron (**Figure 2a**), with seven capping Ag atoms (Ag_{cap}) around the icosahedron surface (**Figure 2b**). Whereas the PtHA_{12} cores in **1** and **2** are similar, the arrangements of the seven Ag_{cap} atoms are different. The difference comes from one of the seven Ag_{cap} atoms which migrates onto another Ag_3 triangle upon going from **1** to **2**. Hence, the PtHA_{19} framework of **1** possesses C_1 symmetry, while it approximates C_3 symmetry in **2**. Similar M_{20} arrangements have been shown to exist in related 8-electron $\text{M}_{20}(\text{dtp}/\text{dsep})_{12}$ NCs, *i.e.*, Ag_{20} (C_1),²⁷ AuAg_{19} (C_1),²⁸ $\text{Cu}_{3.5}\text{Ag}_{16.5}$ (C_1 ²⁹ and C_3 ³⁰), $\text{Cu}_{2.5}\text{AuAg}_{16.5}$ (C_1),³⁰ and Ag_{20} (C_3).^{27,31} However, a distinct feature of **1** and **2** is that their Ag_{12} icosahedron is substantially distorted away from ideal I_h symmetry. This distortion can be described as the enlargement of one of the icosahedral faces with Ag...Ag distances of 3.3143(7), 3.2140(8) and 3.2075(7) Å in the case of **1**, and 3.3653(9), 3.2454(9) and 3.2304(9) Å in the case of **2** (**Figure 2c** and **Figure S1**). Such distortion is also reflected from the continuous symmetry measurement (CSM) values.³² With respect to an ideal icosahedron which has zero CSM value, the calculated CSM for the PtHA_{12} cores in **1** and **2** are 0.16 and 0.15, which are substantially larger than that in the PtAg_{12} core of $\text{PtAg}_{20}(\text{dtp})_{12}$ (0.05).²⁴ It is worth noting that a much larger CSM value (0.27) was found for the RhH@Ag_{12} core of the $[\text{RhH@Ag}_{24}(\text{SPhMe}_2)_{18}]^{2-}$ NC, to reveal a wider open site that suggests the

presence of hydride in the cluster core.⁸ This icosahedral distortion does not much affect the surrounding capping atoms. Although the arrangement and the number of Ag_{cap} atoms in **1** are different from those in PtAg₂₀(dtp)₁₂, the Ag_{cap}-Ag_{ico} distances are similar (avg. 3.0151(6) Å in **1**, avg. 2.9813(9) Å in PtAg₂₀(dtp)₁₂).

The positions of the hydride in **1** and **2** were found from the residual densities in the X-ray data and could be refined with some constraint. Furthermore, a neutron diffraction investigation was carried out on **1** (structure **1N**), confirming unambiguously the hydride position inside a tetrahedron composed of a Pt and the expanded (Ag_{ico})₃ triangular faces (Figure 2d) that contains Ag3, Ag4 and Ag9. The Pt-H distance (1.67(4) Å) is significantly shorter than the Ag_{ico}-H ones (avg. 1.93(5) Å), revealing substantially stronger bonding. The averaged ∠Ag_{ico}-H-Ag_{ico} and ∠Pt-H-Ag_{ico} angles (114(3)° and 104(2)°, respectively) are indicative of a distorted tetrahedral μ₄-H coordination. Thus, the connection of the hydride to a triangular icosahedral face induces its expansion (Figure S1). The encapsulated PtH motif is iso-electronic to Au, in a similar way as the encapsulated RhH motif in [RhHAg₂₄(SR)₁₈]²⁻ is isoelectronic to Pd.⁸ Thus the whole structure in **1** and **2** can be described as an 8-electron [PtH@Ag₁₂]⁵⁺ core protected by an outer [Ag₇(dtp/dsep)₁₂]⁵⁻ shell (Figure 2e). The X-ray structure of **2** located also the hydride connected to Pt and to the expanded icosahedral triangle. As compared to **1**, the different topology in the Ag_{cap} distribution (Figure 2b) induces also different orientations of the surrounding ligands. The twelve ligands in **2** can be grouped into four coordination environments related to C₃ symmetry (Figure 2e, L_A-L_D), with three dsep ligands in each domain. L_A and L_D exhibit η² (μ₂, μ₁) and η³ (μ₂, μ₁) connecting modes, located around the 3-fold axis, at the top and bottom respectively. L_B and L_C are alternatively situated around the belt, exhibiting η³ (μ₂, μ₁) and η³ (μ₂, μ₂) modes, respectively. On the other hand, the twelve dtp ligands in **1** are chemically inequivalent, due to the cluster C₁ symmetry.

The hydride presence is unequivocally confirmed by the ^1H NMR spectra of **1** and **2**, and their hydride resonances in negative values were observed at low frequencies. The hydride chemical shift $\delta(^1\text{H})$ at ambient temperature displays an un-resolved resonance flanked with platinum satellites at -10.8 ppm ($^1J_{\text{PtH}} = 499$ z) for **2** and -12.3 ppm ($^1J_{\text{PtH}} = 491$ Hz) for **1**, respectively (Figure 3 and Figure 4). The VT ^1H NMR experiment of **2** shows a gradually resolved hydride splitting pattern and slightly down-fielded shift upon decreasing the temperature (Figure 3). At 173K only one pseudo quartet centered at -9.7 ppm accompanied by a set of platinum satellite can be seen. The observed splitting pattern results from the hydride coupled to three $^{107}\text{Ag}/^{109}\text{Ag}$ nuclei and one ^{195}Pt nuclei, which is confirmed by its simulated spectrum by using the following parameters: $^1J(^1\text{H}-^{107}\text{Ag}) = 44$ Hz, $^1J(^1\text{H}-^{109}\text{Ag}) = 50$ Hz, $^1J(^1\text{H}-^{195}\text{Pt}) = 502$ Hz (Figure S2). Hence, the NMR spectroscopic result matches perfectly with the hydride coordination environment as revealed by neutron diffraction. *The hydride atom is buried within a (PtAg₃) tetrahedral cavity, coordinating to the central Pt and three Ag_{ico} atoms.* Surprisingly, the VT ^1H NMR experiment of **1** not only shows a gradually resolved hydride splitting pattern but also splits into two pseudo quartets upon lowering the temperature (Figure 4a). The $^1\text{H}\{^{195}\text{Pt}\}$ decoupling experiment removed the effect of overlapped Pt satellites and further confirmed two hydride resonances centered at -11.8 and -12.7 ppm at 173K (Figure 4b). The hydride signal of **1** does not broaden until 193K, while peak broadening of **2** is observed at 253K. A much faster movement of the peripheral Ag_{cap} atoms is assumed in **1**, swapping on the triangular planes of the icosahedron. The result suggests that a rapid exchange process between two isomers of different symmetries occurs at ambient temperature. The molecular motion slows down by lowering the temperature to 173K to observe both isomers in solution. Such a fluxional behavior is also revealed in the VT $^{31}\text{P}\{^1\text{H}\}$ NMR spectrum of **2** (Figure 3b). Two distinct broad resonances at 64.5 and 68.1 ppm were observed at ambient

temperature, suggesting that both C_1 and C_3 isomers of **2** are present in solution. The major resonance resolves into four peaks with approximately equal intensity at 173 K, corresponding to the four coordination environments (L_A - L_D in **Figure 2e**) of the dsep ligands in the pseudo- C_3 solid-state structure of **2**. These results undoubtedly suggest that the two isomers of **2** existing in solution at ambient temperature transform into the more stable pseudo- C_3 form at low temperature. Unfortunately, the VT $^{31}\text{P}\{^1\text{H}\}$ NMR spectrum of **1** (**Figure S3**) shows a complicated un-resolved pattern due to the existence of isomeric mixture at 173K. Thus the isomerization process of **1** monitored by VT $^{31}\text{P}\{^1\text{H}\}$ NMR spectroscopy is not informative.

The $^{195}\text{Pt}\{^1\text{H}\}$ NMR spectrum of **2** exhibits an extraordinary broad resonance ranging from -8320 to -8890 ppm at 293K, and appears at -8798.3 ppm at 173K (**Figure S4**), which is the most up-fielded shift among the reported resonances,³³ such as in $[\text{Pt}(\text{H})(\text{AuPPH}_3)_8]^+$ (-5673 ppm)³⁴ and $[\text{Pt}(\text{H})(\text{AgNO}_3)_2(\text{AuPPH}_3)_8]^{3+}$ (-6348 ppm).³⁵ The $^1\text{H}\{^{195}\text{Pt}\}$ experiments were performed by recording ^1H nuclei decoupled with various ranges of ^{195}Pt magnetic field at 293 K (**Figure S5**). When the decoupling range approaches the signal of Pt, the platinum satellites in the $^1\text{H}\{^{195}\text{Pt}\}$ NMR spectrum disappear, confirming that the hydride is bound to the Pt atom. On the other hand, the $^{195}\text{Pt}\{^1\text{H}\}$ NMR spectrum of **1** (**Figure 4c**) at 293K shows a broad singlet at -8800 ppm due to the rapid movement of the whole molecule, suggesting the existence of fluxional behavior similar to those observed in both $^{31}\text{P}\{^1\text{H}\}$ and $^1\text{H}\{^{31}\text{P}\}$ spectra. It further splits into two singlets at -8753.6 and -8869.7 ppm upon decreasing the temperature, indicating the presence of two isomers probably those of C_1 and C_3 symmetries. The $^1\text{H}\{^{195}\text{Pt}\}$ NMR spectra of **1** at 293K recorded under various ^{195}Pt decoupling ranges show a similar pattern as **2** (**Figure S6**). The $^1\text{H}\{^{195}\text{Pt}\}$ experiments at 173K (**Figure S7**) confirm that the more down-fielded resonance at -11.7 ppm is related to the more up-fielded resonance at -8869.7 ppm in the $^{195}\text{Pt}\{^1\text{H}\}$ spectrum, and *vice versa*.

Considering both coupling constants $^1J(^1\text{H}-^{107}\text{Ag})$ and $^1J(^1\text{H}-^{109}\text{Ag})$ related to -12.5 ppm in **1** at 173 K (Figure 4a), they are the same as those in the ^1H NMR spectrum of **2** at 173 K (Figure 3a), indicating a highly similar environment for the interstitial hydride. Therefore, the resonance at -11.7 ppm with higher intensity can be assigned to the cluster of C_1 symmetry, and the minor resonance could be its C_3 isomer.

The UV-Vis absorption spectrum of **1** (Figure 5a) depicts one major absorption band centered at 419 nm, which is similar to that of $[\text{PtAg}_{20}\{\text{S}_2\text{P}(\text{O}^i\text{Pr})_2\}_{12}]$ (412 nm).²⁴ **2** exhibits two absorption bands at 388 and 468 nm (Figure 5b), slightly red-shifted compared with **1**. In addition, we found that the ligand nature can enhance the photoluminescence (PL) properties. Compound **1** did not exhibit any PL even at 77K, but its Se analogue **2** displayed a strong PL (636 nm) at 77K. The lifetime of **2** (~11 μs) suggests phosphorescence (Figure S8).

Compound **1** is thermally stable at ambient temperature in THF- d_8 solution, as shown by the permanence of their ^{31}P NMR spectra during a 3-month period (Figure S9). However, the persistence of **1** in chloro-solvents is not as good and partial decompositions into $[\text{PtAg}_{20}\{\text{S}_2\text{P}(\text{O}^i\text{Pr})_2\}_{12}]$ and $[\text{Ag}\{\text{S}_2\text{P}(\text{O}^i\text{Pr})_2\}]_n$ in CDCl_3 at room temperature was observed after 4 days (Figure S10).

Compounds **1** and **2**, were investigated by DFT calculations at the BP86/Def2-TZVP level of calculations (see Computational Details in the SI). For the sake of computational limitations, the dtp and dsep ligands were replaced by S_2PH_2 and Se_2PH_2 models, respectively, a simplification which has been proved to be reasonable in many past investigations.^{17,18,20,21,24,26-28,29} For each ligand, both C_1 and C_3 structures were considered. The resulting computed models are labelled **1'**(C_1), **1'**(C_3), **2'**(C_1) and **2'**(C_3) in the followings. It is of note that the C_1 and C_3 isomers of **1'** and **2'** provided very similar computed results. This is exemplified by their very close total energy differences (0.6 kcal/mol for **1'** and 1.7 kcal/mol for **2'**, the C_3 isomer being the most stable in both

species) and free energy differences (1.8 and 0.8 kcal/mol, respectively). At our level of modeling, these energy differences are barely significantly different from zero, thus supporting the fact that both isomers can coexist in solution.

Selected computed data are given in [Table 1](#), [Table 2](#) and [Table S3](#). The computed metrics of **1'**(C₁) and **2'**(C₃) ([Table 1](#)) are in good agreement with their experimental counterparts, with a small overestimation (lower than 3%) of bond distances. In particular, the icosahedron distortion and the μ_4 coordination mode of the hydride are well reproduced. In the four models, both Pt and H are negatively charged ([Table 2](#)), although the charge of H is significantly lower than that found usually for typical hydrides, for example -0.65 in [Ag₇(H)(S₂PH₂)₆].³⁶ The Wiberg bond indices are consistent with the existence of significant Pt-H covalent bonding and weaker, but non-negligible, Ag-H bonding. The Pt-Ag and Ag...Ag interactions are of the same order of magnitude as those found in the relative 8-electron [PtAg₂₀(S₂PH₂)₁₂] ([see Table 2](#)). Owing to the similarities between the four computed models, we only describe below the electronic structure of **1'**(C₃). Its Kohn-Sham orbital diagram is shown in [Figure 6](#) besides that of the 8-electron [Ag₂₀(S₂PH₂)₁₂] and [PtAg₂₀(S₂PH₂)₁₂] models. The frontier orbitals of the three models are plotted in [Figure S11](#). One goes from [Ag₂₀(S₂PH₂)₁₂] to **1'** by replacing the encapsulated Ag in the former by an isoelectronic Pt-H unit in the latter. One goes from **1'** to [PtAg₂₀(S₂PH₂)₁₂] by removing the encapsulated H in the former and adding a supplementary capping (outer) Ag atom in the latter. The diagrams of [Figure 6](#) clearly show similar electronic features for the three compounds. Their three highest occupied orbitals can be easily identified as the 1P *superatomic* orbitals (with 2% H participation in the case of **1'**) and their five lowest vacant ones to the 1D levels ([see Figure S11](#)). For the three clusters, a unique 1S orbital cannot be identified, due to substantial mixing with metal d-type combinations. Thus, despite its distorted icosahedral core, **1'** is, like its [Ag₂₀(S₂PH₂)₁₂] and

[PtAg₂₀(S₂PH₂)₁₂] congeners, an 8-electron *superatoms*.

In order to analyze more deeply the role played by the encapsulated hydride in the electronic structure of **1'** and **2'**, calculations were carried out on their bare *superatomic* core [PtHAg₁₂]⁵⁺ (selected results in Table 2). Its optimized structure, of C_{3v} symmetry (Figure S12), matches reasonably well with that of **1'** and **2'** (Pt-H = 1.653, Ag-H = 2.238, Pt-Ag(av.) = 2.982 Å), except from the fact that, owing to its large cationic charge, free [PtHAg₁₂]⁵⁺ is more expanded than when stabilized as the passivated core of **1'**. Its charge distribution and Wiberg indices are consistent with those of **1'** and **2'**. Its electronic structure can be rationalized on the basis of the interaction between the [PtAg₁₂]⁵⁺ cage and its encapsulated hydrogen atom, as sketched in the qualitative MO diagram of Figure 7. Considered as isolated, the 7-electron [PtAg₁₂]⁵⁺ fragment is an unstable electron-deficient *superatom*. However, it reaches closed-shell stability by encapsulating the H-atom, through interaction of its 5d_z²(Pt) orbital with the 1s(H) AO (assuming the z and C₃ axes colinear), leading to the formation of an occupied Pt-H bonding orbital and a vacant antibonding combination that provokes the complete filling of the 1P shell. Thus, [PtHAg₁₂]⁵⁺ is an 8-electron *superatom* that contains an encapsulated Pt-H unit. Of course, the 2 electrons associated with the Pt-H bond get somewhat delocalized onto the whole cluster cage, through some participation to the *superatomic* orbitals of the 1s(H) and, to a lesser extent, the 5d_z²(Pt) orbitals. Going from [PtAg₂₀(S₂PH₂)₁₂] to **1'** corresponds to the replacement of a 5d_z²(Pt) lone pair in the former by a σ(Pt-H) bonding pair in the latter. Of course, this rather low-lying σ(Pt-H) orbitals is also present in **1'** (see Figure 6), with Pt, H and Ag₁₂ participation of 15, 44 and 39%, respectively. In both [PtAg₂₀(S₂PH₂)₁₂] and **1'**, the electron pair in question is (moderately) involved in cluster bonding; weakly in the case of 5d_z²(Pt) of [PtAg₂₀(S₂PH₂)₁₂]³⁷⁻³⁹ and somewhat more importantly in the case of σ(Pt-H) in **1'**. This stronger bonding in the latter case helps compensating the energy loss upon

distortion of the icosahedral cage.

Consistently with the fact that the electron of the encapsulated hydrogen participates to the *superatom* electron count, adding two supplementary electrons to $[\text{PtHAg}_{12}]^{5+}$, *i.e.* making $[\text{PtHAg}_{12}]^{3+}$ results in a structure in which the hydride is expelled outside the cage to become a regular $\mu_3\text{-H}$ outer ligand (see Figure S12). Thus, the $[\text{PtHAg}_{12}]^{3+}$ model consists of a regular 8-electron $[\text{PtAg}_{12}]^{4+}$ *superatomic* core, “protected” by one capping hydride.

The TD-DFT UV-Vis spectra simulated at the CAM-B3LYP/Def2-TZVP level (see Computational Details in the SI) of both the C_1 and C_3 isomers of **1'** and **2'** are shown together with the recorded spectra of **1** and **2** in Figure 5. The spectra show little difference between isomers and there is a good overall agreement between them and their experimental counterparts. The low-energy bands are associated with $1\text{P}\rightarrow 1\text{D}$ transitions, as in the $[\text{PtAg}_{20}(\text{dtp}/\text{desp})_{12}]$ and $[\text{Ag}_{20}(\text{dtp}/\text{desp})_{12}]$ species.

Conclusion

In summary, two hydride-containing 8-electron Pt/Ag alloy NCs, $[\text{PtHAg}_{19}\{\text{S}_2\text{P}(\text{O}^i\text{Pr})_2\}_{12}]$ (**1**) and $[\text{PtHAg}_{19}\{\text{Se}_2\text{P}(\text{O}^i\text{Pr})_2\}_{12}]$ (**2**), were successfully isolated and the LEIST method was used to synthesize **2** via the reaction of **1** with dsep ligands. The former compound is the first hydride-containing 8-e *superatom*, of which the structure was fully ascertained by neutron diffraction. The encapsulated hydride leads to the expansion of one triangular face of the icosahedron and sits inside the tetrahedron formed by this face and the central Pt atom. The electron of the interstitial hydride participates in the $[\text{PtH@Ag}_{12}]^{5+}$ *superatomic* electron count, which is isoelectronic to $[\text{Au@Ag}_{12}]^{5+}$. On the other hand, the $1s(\text{H})$ orbital participates only moderately to the *superatomic* orbitals, but more importantly to the building of a Pt-H bonding orbital with the $5d_z^2(\text{Pt})$ orbital. The hydride coordination environment is in

good agreement with the NMR spectroscopy. Whereas the solid-state structure of **1** is of C_1 symmetry, that of **2** is C_3 . This difference originates from slightly different configurations in their outer spheres. Both VT ^1H and $^{31}\text{P}\{^1\text{H}\}$ NMR spectra of **2** show that isomers with different symmetries co-exist in solution at ambient temperature and the isomer of C_3 symmetry is a dominant structure at 173 K, in agreement with the DFT results. Moreover, an enhancement of photoluminescence is also observed after structure distortion induced by ligand exchange of sulfur-donors (dtp) by selenium-donor ligands (dsep).

References

1. Jin, R.; Zeng, C.; Zhou, M.; Chen, Y. Atomically Precise Colloidal Metal Nanoclusters and Nanoparticles: Fundamentals and Opportunities. *Chem. Rev.*, **2016**, *116*, 10346-10413.
2. Chakraborty, I.; Pradeep, T. Atomically Precise Clusters of Noble Metals: Emerging Link between Atoms and Nanoparticles. *Chem. Rev.*, **2017**, *117*, 8208-8271.
3. Wang, Q.-M.; Lin, Y.-M.; Liu, K.-G. Role of Anions Associated with the Formation and Properties of Silver Clusters *Acc. Chem. Res.*, **2015**, *48*, 1570-1579.
4. Parker, J. F.; Fields-Zinna, C. A.; Murray, R. W. The Story of a Monodisperse Gold Nanoparticle: $\text{Au}_{25}\text{L}_{18}$. *Acc. Chem. Res.*, **2010**, *43*, 1289-1296.
5. Jin, R.; Nobusada, K. Doping and alloying in atomically precise gold nanoparticles. *Nano Res.*, **2014**, *7*, 285-300.
6. Sharma, S.; Chakraborty, K. K.; Saillard, J. Y.; Liu, C. W. Structurally Precise Dichalcogenolate-Protected Copper and Silver Superatomic Nanoclusters and Their Alloys. *Acc. Chem. Res.*, **2018**, *51*, 2475-2483.
7. Yuan, X.; Sun, C.; Li, X.; Malola, S.; Teo, B. K.; Häkkinen, H.; Zheng, L.-S.;

- Zheng, N. Combinatorial Identification of Hydrides in a Ligated Ag₄₀ Nanocluster with Noncompact Metal Core. *J. Am. Chem. Soc.* **2019**, *141*, 11905–11911.
8. Yi, H.; Han, S. M.; Song, S.; Kim, M.; Sim, E.; Lee, D. Superatom-in-Superatom [RhH@Ag₂₄(SPhMe₂)₁₈]²⁻ Nanocluster *Angew. Chem., Int. Ed.* **2021**, *60*, 22293–22300.
9. Takano, S.; Hirai, H.; Muramatsu, S.; Tsukuda, T. Hydride-Doped Gold Superatom (Au₉H)²⁺: Synthesis, Structure, and Transformation. *J. Am. Chem. Soc.* **2018**, *140*, 8380–8383.
10. Takano, S.; Hirai, H.; Muramatsu, S.; Tsukuda, T. Hydride-Mediated Controlled Growth of a Bimetallic (Pd@Au₈)²⁺ Superatom to a Hydride-Doped (HPd@Au₁₀)³⁺ Superatom. *J. Am. Chem. Soc.* **2018**, *140*, 12314–12317.
11. Yuan, S.-F.; Li, J.-J.; Guan, Z.-J.; Lei, Z.; Wang, Q.-M. Ultrastable Hydrido Gold Nanoclusters with the Protection of Phosphines. *Chem. Commun.* **2020**, *56*, 7037–7040.
12. Dong, J.; Gao, Z.-H.; Wang, L.-S. The synthesis and characterization of a new diphosphine-protected gold hydride nanocluster. *J. Chem. Phys.* **2021**, *155*, 034307.
13. Dong, J.; Gao, Z.-H.; Zhang, Q.-F.; Wang, L.-S. The Synthesis, Bonding, and Transformation of a Ligand-Protected Gold Nanohydride Cluster. *Angew. Chem., Int. Ed.* **2021**, *60*, 2424–2430.
14. Wei, X.; Kang, X.; Duan, T.; Li, H.; Wang, S.; Pei, Y.; Zhu, M. [Au₁₆Ag₄₃H₁₂(SPhCl₂)₃₄]⁵⁻: An Au–Ag Alloy Nanocluster with 12 Hydrides and Its Enlightenment on Nanocluster Structural Evolution. *Inorg. Chem.* **2021**, *60*, 11640–11647.
15. Zhu, C.; Duan, T.; Li, H.; Wei, X.; Kang, X.; Pei, Y.; Zhu, M. Structural

- determination of a metastable Ag₂₇ nanocluster and its transformations into Ag₈ and Ag₂₉ nanoclusters. *Inorg. Chem. Front.*, **2021**, *8*, 4407-4414.
16. Ito, E.; Takano, S.; Nakamura, T.; Tsukuda, T. Controlled Dimerization and Bonding Scheme of Icosahedral M@Au₁₂ (M=Pd, Pt) Superatoms *Angew. Chem., Int. Ed.* **2020**, *133*, 655-659.
 17. Zhong, Y.-J.; Liao, J.-H.; Chiu, T.-H.; Kahlal, S.; Lin, C.-J.; Saillard, J.-Y.; Liu, C.-W. A Two-Electron Silver Superatom Isolated from Thermally Induced Internal Redox Reactions of a Silver(I) Hydride. *Angew. Chem., Int. Ed.* **2021**, *60*, 12712– 12716.
 18. Charkrahari, K. K.; Liao, J.; Silalahi, R. P. B.; Chiu, T.-H.; Liao, J.-H.; Wang, X.; Kahlal, S.; Saillard, J.-Y.; Liu, C. W. Isolation and Structural Elucidation of 15-Nuclear Copper Dihydride Clusters: An Intermediate in the Formation of a Two-Electron Copper Superatom. *Small* **2021**, *17*, 2002544.
 19. van Zyl, W. E.; Liu, C. W. Interstitial Hydrides in Nanoclusters can Reduce M(I) (M=Cu, Ag, Au) to M(0) and Form Stable Superatoms. *Chem. Eur. J.* **2022**, *28*, e202104241.
 20. Silalahi, R. P. B.; Wang, Q.; Liao, J.-H.; Chiu, T.-H.; Wu, Y.-Y.; Wang, X.; Kahlal, S.; Saillard, J.-Y.; Liu, C. W. Reactivities of Interstitial Hydrides in a Cu₁₁ Template: En Route to Bimetallic Clusters. *Angew. Chem. Int. Ed.* **2022**, *61*, e202113266.
 21. Silalahi, R. P. B.; Huang, G.-R.; Liao, J.-H.; Chiu, T.-H.; Charkrahari, K. K.; Wang, X.; Cartron, J.; Kahlal, S.; Saillard, J.-Y.; Liu, C. W. *Inorg. Chem.* **2020**, *59*, 2536-2547.
 22. Knng X.; Zhu, M. Transformation of Atomically Precise Nanoclusters by Ligand-Exchange. *Chem. Mater.* **2019**, *31*, 9939-9969.

23. Dhayal, R. S.; Liao, J.-H.; Wang, X.; Liu, Y.-C.; Chiang, M.-H.; Kahlal, S.; Saillard, J.-Y.; Liu, C. W. Diselenophosphates Induced Conversion of An Achiral $[\text{Cu}_{20}(\text{H})_{11}\{\text{S}_2\text{P}(\text{O}^i\text{Pr})_2\}_9]$ into A Chiral $[\text{Cu}_{20}(\text{H})_{11}\{\text{Se}_2\text{P}(\text{O}^i\text{Pr})_2\}_9]$ Polyhydrido Nanocluster. *Angew. Chem. Int. Ed.* **2015**, *54*, 13604-13608.
24. Chiu, T.-H.; Liao, J.-H.; Gam, F.; Chantrenne, I.; Kahlal, S.; Saillard, J.-Y.; Liu, C. W. Homoleptic Platinum/Silver Superatoms Protected by Dithiolates: Linear Assemblies of Two and Three Centered Icosahedra Isolobal to Ne_2 and I_3^- . *J. Am. Chem. Soc.* **2019**, *141*, 12957–12961.
25. Chiu, T.-H.; Liao, J.-H.; Gam, F.; Chantrenne, I.; Kahlal, S.; Saillard, J.-Y.; Liu, C. W. All-selenolate-protected eight-electron platinum/silver nanoclusters *Nanoscale*, **2021**, *13*, 12143-12148.
26. Barik, S. K.; Chiu, T. H.; Liu, Y. C.; Chiang, M. H.; Gam, F.; Chantrenne, I.; Kahlal, S.; Saillard, J. Y.; Liu, C. W. Mono- and Hexa-Palladium Doped Silver Nanoclusters Stabilized by Dithiolates. *Nanoscale* **2019**, *11*, 14581–14586.
27. Dhayal, R. S.; Lin, Y. R.; Liao, J. H.; Chen, Y. J.; Liu, Y. C.; Chiang, M. H.; Kahlal, S.; Saillard, J. Y.; Liu, C. W. $[\text{Ag}_{20}\{\text{S}_2\text{P}(\text{OR})_2\}_{12}]$: A superatom complex with a chiral metallic core and high potential for isomerism. *Chem. - Eur. J.* **2016**, *22*, 9943– 9947.
28. Lin, Y.-R.; Kishore, P. V. V. N.; Liao, J.-H.; Kahlal, S.; Liu, Y.-C.; Chiang, M.-H.; Saillard, J.-Y.; Liu, C. W. Synthesis, structural characterization and transformation of an eight-electron superatomic alloy, $[\text{Au}@\text{Ag}_{19}\{\text{S}_2\text{P}(\text{OPr})_2\}_{12}]$ *Nanoscale* **2018**, *10*, 6855-6860.
29. Zhong, Y.-J.; Liao, J.-H.; Chiu, T.-H.; Gam, F.; Kahlal, S.; Saillard, J.-Y.; Liu, C. W. Doping effect on the structure and properties of eight-electron silver nanoclusters. *J. Chem. Phys.* **2021**, *155*, 034304.
30. Yen, W.-J.; Liao, J.-H.; Chiu, T.-H.; Wen, Y.-S.; Liu, C. W. A Homoleptic

- Silver-Rich Trimetallic M20 Nanocluster. *Inorg. Chem.* **2022**, in revision.
31. Chang, W.-T.; Sharma, S.; Liao, J.-H.; Kahlal, S.; Liu, Y.-C.; Chiang, M.-H.; Saillard, J.-Y.; Liu, C. W. Hereroatom-Doping Increases Cluster Nuclearity: From An [Ag₂₀] to An [Au₃Ag₁₈] Core. *Chem. Eur. J.* **2018**, *24*, 14352-14357.
 32. Zabrodsky, H.; Peleg, S.; Avnir, D. Continuous Symmetry Measures. *J. Am. Chem. Soc.* **1992**, *114*, 7843– 7851.
 33. Still, B. M.; Kumar, P. G. A.; Aldrich-Wright, J. R.; Price, W. S. ¹⁹⁵Pt NMR-theory and application. *Chem. Soc. Rev.* **2007**, *36*, 665–686.
 34. Bour, J. J.; Schlebos, P. P. J.; Kanters, R. P. F.; Schoondergang, M. F. J.; Addens, H.; Overweg, A.; Steggerda, J. J. Hydride platinum gold clusters: synthesis and characterization. *Inorg. Chem. Acta.* **1991**, *181*, 195-200.
 35. Kappen T. G. M. M.; Schlebos, P. P. J.; Bour, J. J.; Bosman, W. P.; Beurskens, G.; Smits, J. M. M.; Beurskens, P. T.; Steggerda, J. J. Cluster Growth: Some Representative Reactions. Crystal Structures of [Pt(H)(AgNO₃)(AuPPh₃)₈](NO₃) and [Pt(H)(AgNO₃)₂(AuPPh₃)₈](NO₃). *Inorg. Chem.* **1995**, *34*, 2121-2132.
 36. Liu, C. W.; Lin, Y. R.; Fang, C. S.; Latouche, C.; Kahlal, S.; Saillard, J. Y. [Ag₇(H){E₂P(OR)₂}]₆ (E = Se, S): Precursors for the Fabrication of Silver Nanoparticles. *Inorg. Chem.* **2013**, *52*, 2070-2077.
 37. Alkan, F.; Pandeya, P.; Aikens, C. M. Understanding the Effect of Doping on Energetics and Electronic Structure for Au₂₅, Ag₂₅, and Au₃₈ Clusters. *J. Phys. Chem. C* **2019**, *123*, 9516-9527.
 38. Wei, J.; Rodríguez-Kessler, P. L.; Halet, J.-F.; Kahlal, S.; Saillard, J.-Y.; Muñoz-Castro, A. On Heteronuclear Isoelectronic Alternatives to [Au₁₃(dppe)₅Cl₂]³⁺: Electronic and Optical Properties of the 18-Electron Os@[Au₁₂(dppe)₅Cl₂] Cluster from Relativistic Density Functional Theory Computations. *Inorg. Chem.* **2021**, *60*, 8173– 8180.

39. Gam, F.; Chantrenne, I.; Kahlal, S.; Chiu, T.-H.; Liao, J.-H.; Liu, C. W.; Saillard, J.-Y. Alloying dichalcogenolate-protected Ag₂₁ eight-electron nanoclusters: a DFT investigation. *Nanoscale* **2012**, *14*, 196-203.

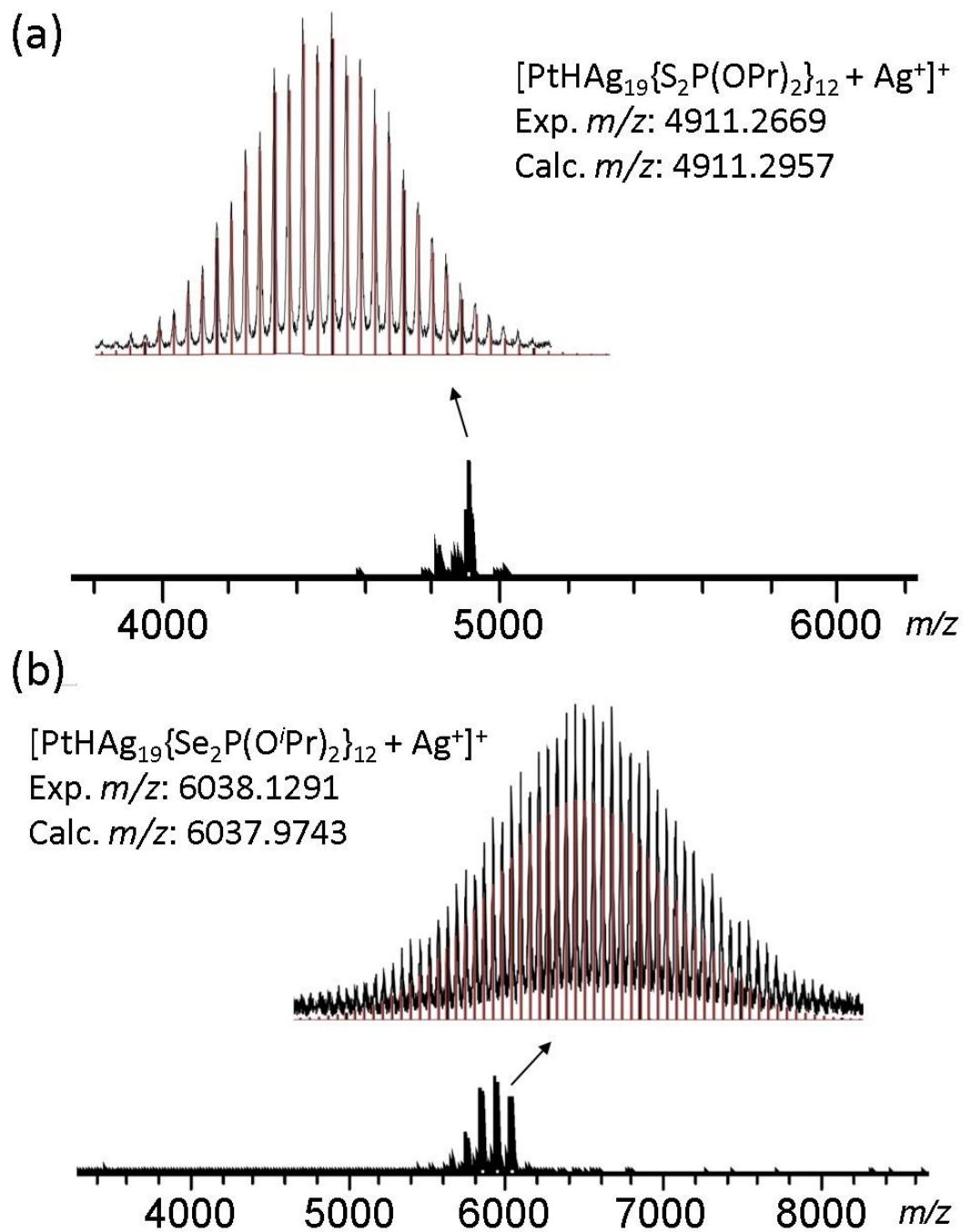


Figure 1. (a) Positive-mode ESI mass spectrum of **1**. Insets: experimental (black) and simulated (red) isotopic distribution of the ion peak $[\mathbf{1} + \text{Ag}^+]^+$. (b) Positive-mode ESI mass spectrum of **2**. Insets: experimental (black) and simulated (red) isotopic distribution of the ion peak $[\mathbf{2} + \text{Ag}^+]^+$.

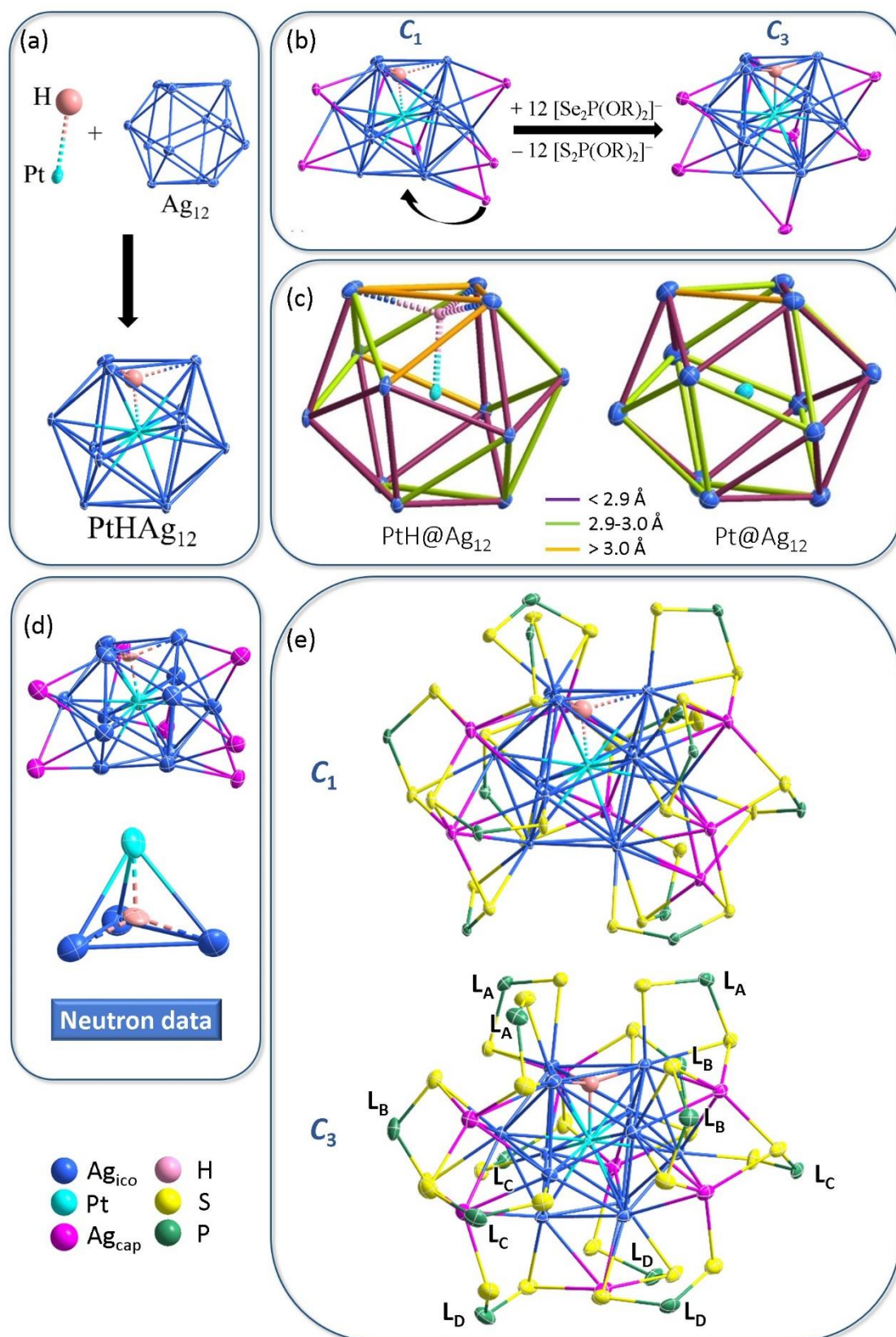


Figure 2. (a) The “PtH” unit enclosed in the Ag_{12} icosahedral skeleton. (b) The metal framework of **1** (left) and **2** (right). (c) A schematic representation of the $\text{Ag}_{\text{ico}}\text{-Ag}_{\text{ico}}$ distance distributions in **1** (PtH@Ag_{12} , left) and $[\text{PtAg}_{20}\{\text{S}_2\text{P}(\text{O}^i\text{Pr})_2\}_{12}]$ (Pt@Ag_{12} ,

right). (d) The neutron structure (**1_N**, top) and the coordination environment of hydride (bottom). (e) The total structures of **1** (left) and **2** (right), with -OR groups omitted for clarity. Thermal ellipsoids were drawn at 50% probability. Color code: pink, H; cyan, Pt; blue, Ag_{ico}; magenta, Ag_{cap}; yellow, S or Se; green, P.

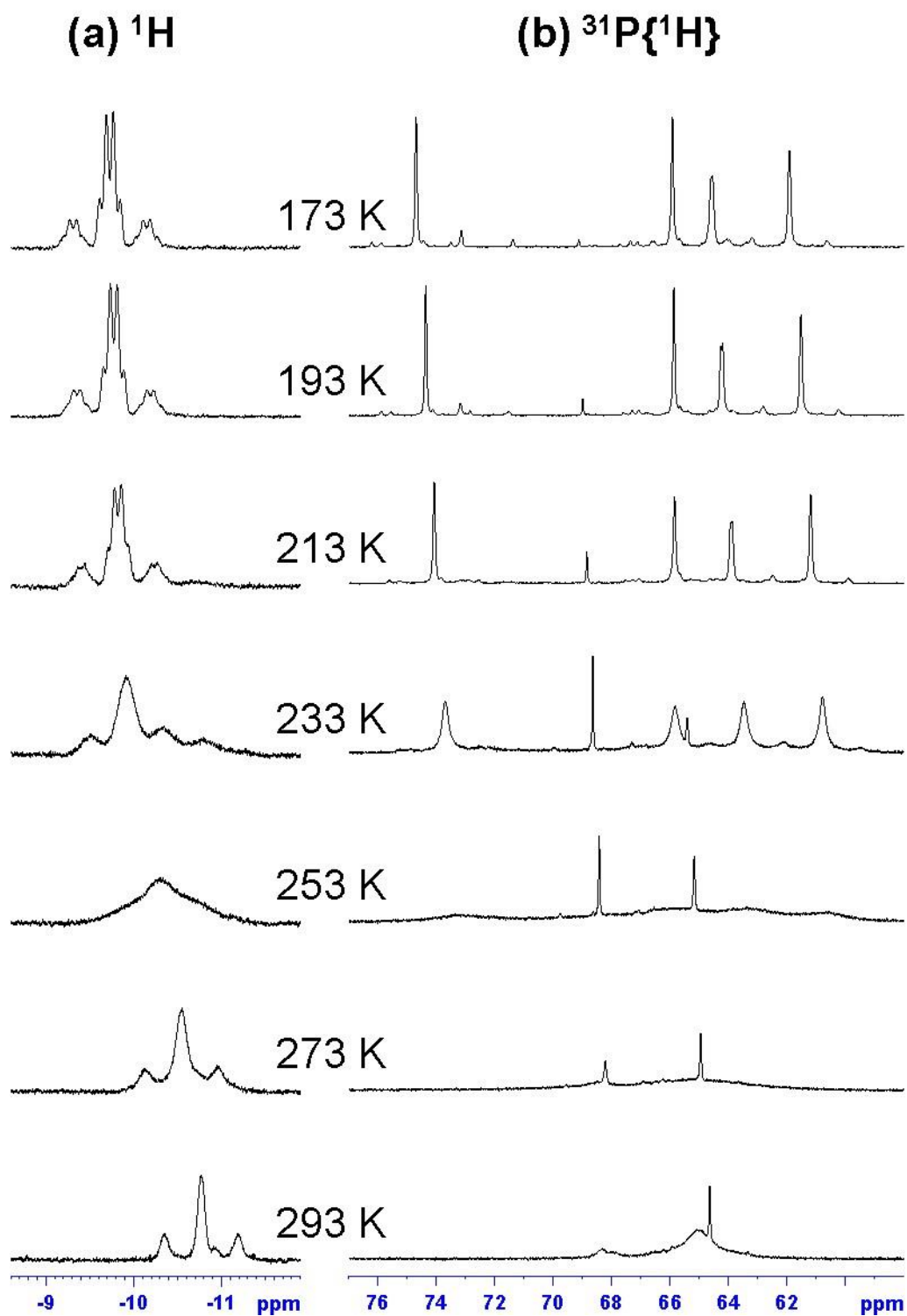


Figure 3. (a) The VT ^1H NMR (THF-d_8 , δ , ppm) of **2**. The hydride resonance: -10.8 ($^1J_{\text{H-195Pt}} = 499$ Hz at 293K), -9.7 ($^1J_{\text{H-195Pt}} = 502$ Hz, $^1J_{\text{H-107Ag}} = 44$ Hz, $^1J_{\text{H-109Ag}} = 50$ Hz at 173K), and (b) VT $^{31}\text{P}\{^1\text{H}\}$ spectra of **2**.

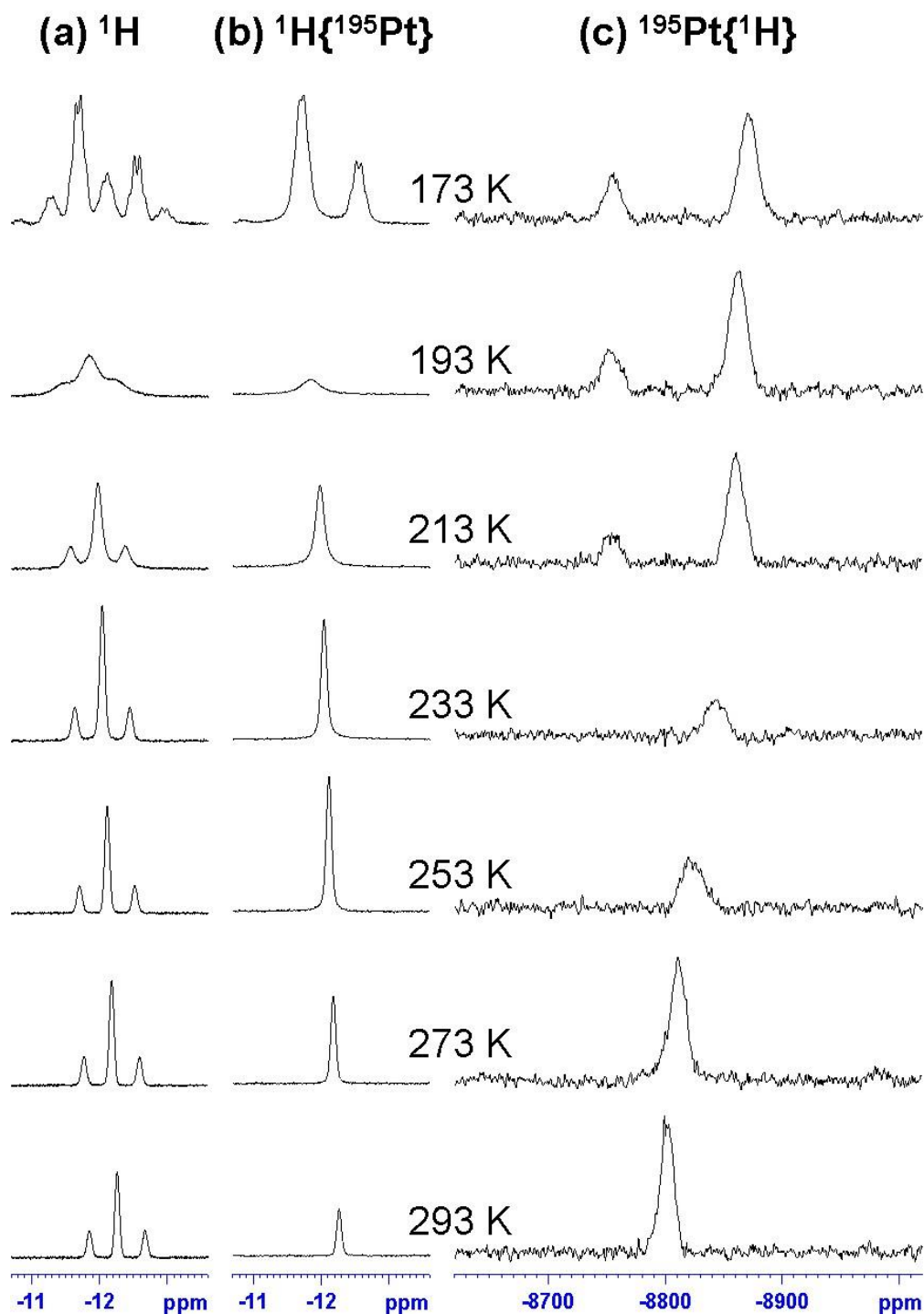


Figure 4. (a) VT ^1H NMR (THF- d_8 , δ , ppm) spectra. The hydride resonance: -12.3 ($^1J_{\text{H-}^{195}\text{Pt}} = 491$ Hz at 293K), -11.7 ($^1J_{\text{H-}^{195}\text{Pt}} = 485$ Hz, $^1J_{\text{H-}^{107}\text{Ag}} = 37$ Hz, $^1J_{\text{H-}^{109}\text{Ag}} = 43$ Hz at 173K) and -12.5 ($^1J_{\text{H-}^{195}\text{Pt}} = 485$ Hz, $^1J_{\text{H-}^{107}\text{Ag}} = 44$ Hz, $^1J_{\text{H-}^{109}\text{Ag}} = 50$ Hz at 173K), (b) VT $^1\text{H}\{^{195}\text{Pt}\}$, and (c) VT $^{195}\text{Pt}\{^1\text{H}\}$ NMR spectra of **1**.

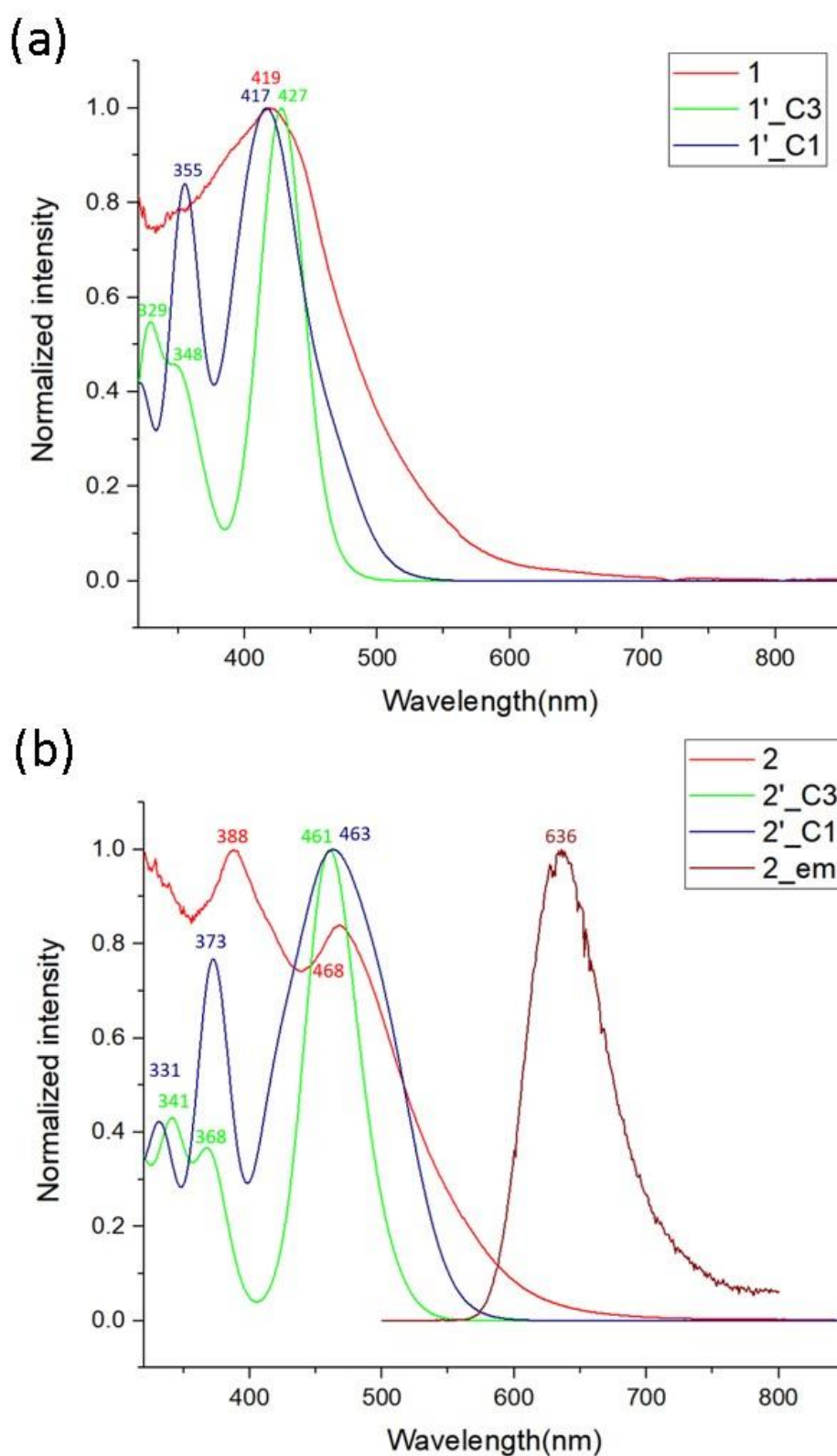


Figure 5. (a) Absorption spectra of **1** (red), **1'** (C₁, blue), and **1'** (C₃, green). (b) Absorption spectra of **2** (red), **2'** (C₃, green), **2'** (C₁, blue), and emission spectrum of **2** (brown).

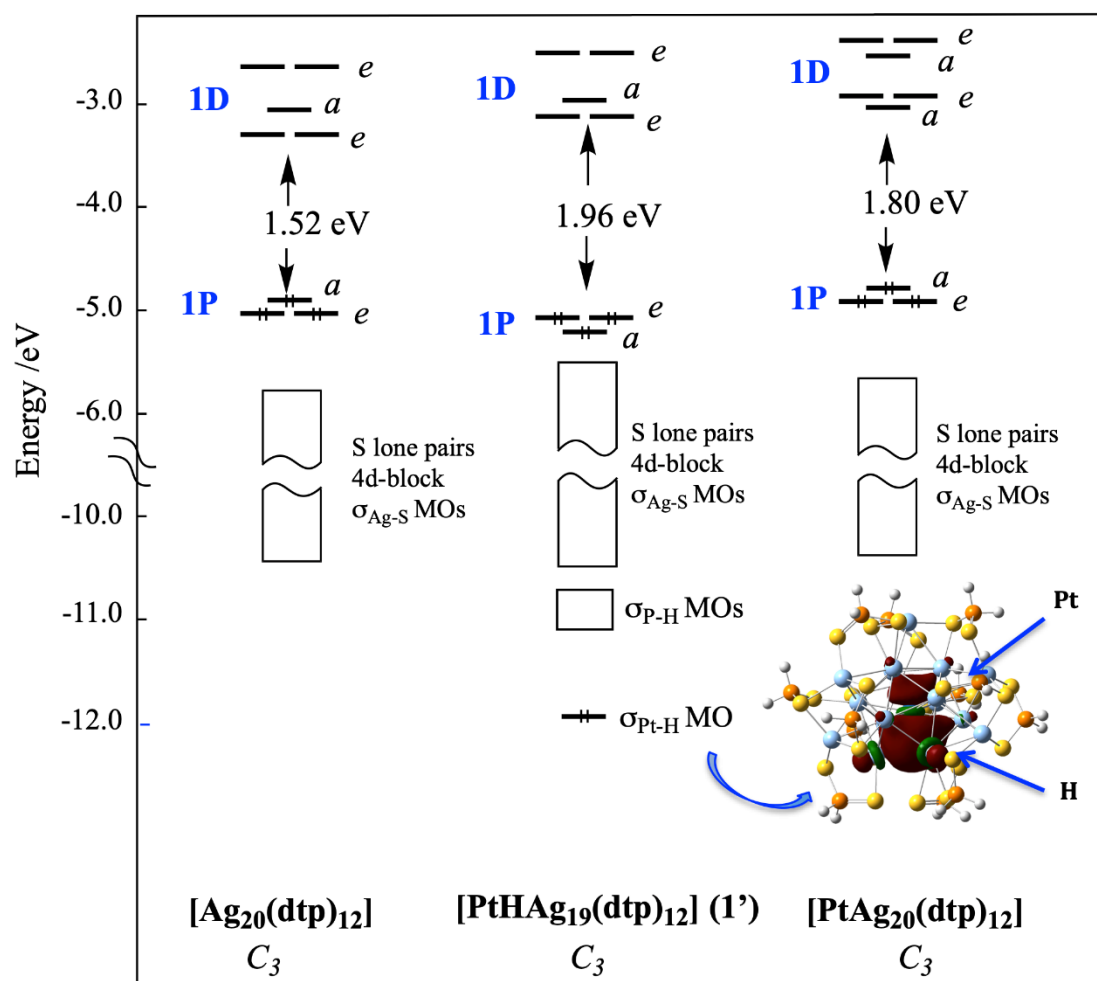


Figure 6. Kohn-Sham orbital diagrams of the models $[\text{Ag}_{20}(\text{dtp})_{12}]$, $[\text{PtHAg}_{19}(\text{dtp})_{12}]$ (1') and $[\text{PtAg}_{20}(\text{dtp})_{12}]$ (dtp = S_2PH_2).

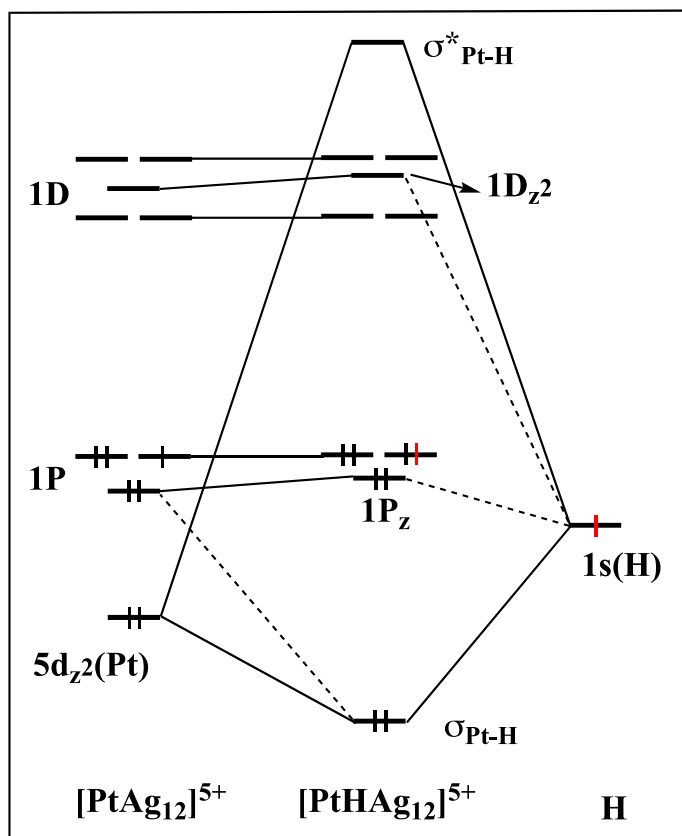


Figure 7. Simplified interaction MO diagram for the 8-electron $[\text{PtHAg}_{12}]^{5+}$ superatom.

Table 1. Selected experimental bond distances (Å) and angles (deg.) for **1**, **1_N**, [PtAg₂₀{S₂P(O^{*o*}Pr)₂}₁₂], **2**, and [PtAg₂₀{Se₂P(O^{*o*}Pr)₂}₁₂], and DFT-optimized counterparts in **1'**(C₁) and **2'**(C₁).

	[PtHAg ₁₉ {S ₂ P(O ^{<i>o</i>} Pr) ₂ } ₁₂] (1 , X-ray)	[PtHAg ₁₉ {S ₂ P(O ^{<i>o</i>} Pr) ₂ } ₁₂] (1_N , neutron)	[PtHAg ₁₉ (S ₂ PH ₂) ₁₂] (1' , DFT)	[PtAg ₂₀ {S ₂ P(O ^{<i>o</i>} Pr) ₂ } ₁₂]	[PtHAg ₁₉ {Se ₂ P(O ^{<i>o</i>} Pr) ₂ } ₁₂] (2)	[PtHAg ₁₉ (Se ₂ PH ₂) ₁₂] (2' , DFT)	[PtAg ₂₀ {Se ₂ P(O ^{<i>o</i>} Pr) ₂ } ₁₂]
symmetry	C ₁	C ₁	C ₁	C ₂	C ₃	C ₃	T
CSM	0.15	0.16	0.17	0.05	0.15	0.13	0.02
M _{cent} -Ag _{ico}	2.7470(5)–2.8726(5) avg. 2.7984(5)	2.73(2)–2.88(3) avg. 2.80(3)	2.852–2.981 avg. 2.894	2.7034(7)–2.8182(7) avg. 2.7601(7)	2.7621(7)–2.9033(7) avg. 2.8088(7)	2.843–2.933 avg. 2.897	2.7494(15)–2.7601(14) avg. 2.756(4)
Ag _{ico} -Ag _{ico}	2.8246(6)–3.3143(7) avg. 2.9422(6)	2.83(3)–3.29(3) avg. 2.95(3)	2.933–3.474 avg. 3.044	2.8314(9)–3.0135(9) avg. 2.9022(9)	2.8544(9)–3.3653(9) avg. 2.9540(9)	2.975–3.379 avg. 3.047	2.8349(16)–2.9556(16) avg. 2.901(9)
Ag _{ico} -Ag _{cap}	2.8840(6)–3.0976(6) avg. 3.0151(6)	2.88(3)–3.10(3) avg. 3.01(3)	3.040–3.221 avg. 3.1206	2.8601(10)–3.1070(9) avg. 2.9785(9)	2.9120(9)–3.0646(9) avg. 2.9813(9)	3.065–3.217 avg. 3.109	2.9050(18)–2.9956(19) avg. 2.949(9)
H-Pt	1.6702(2)	1.67(4)	1.699		1.80(12)	1.692	
H-Ag _{ico}	1.7749(5)–2.0340(4) avg. 1.9416(5)	1.90(5)–1.97(5) avg. 1.93(5)	2.013–2.036 avg. 2.023		1.799(10)–2.10(12) avg. 1.94(9)	2.034–2.034 avg. 2.034	
Ag _{ico} -H-Ag _{ico}	105.0(1)–121.8(1) avg. 113.8(1)	110(3)–119(3) avg. 114(3)	107.0–118.9 avg. 113.5		102(5)–128(6) avg. 113(5)	112.3–112.3 avg. 112.3	
Pt-H-Ag _{ico}	100.2(1)–110.5(1) avg. 104.2(1)	101(2)–107(2) avg. 104(2)	102.1–106.5 avg. 104.9		94(5)–114(6) avg. 104(5)	106.5–106.5 avg. 106.5	

Table 2. Selected computed data for **1'(C₁)**, **1'(C₃)**, **2'(C₁)** and **2'(C₃)** and related species.

		[PtHAg ₁₂] ⁵⁺	1'(C ₁)	1'(C ₃)	[PtAg ₂₀ (S ₂ PH ₂) ₁₂] (C ₃)	2'(C ₁)	2'(C ₃)
HOMO-LUMO gap (eV)		2.74	1.71	1.96	1.80	1.48	1.69
C ₁ vs. C ₃ relative energy (kcal/mol)			0.6	0.0		1.7	0.0
C ₁ vs. C ₃ relative free energy (kcal/mol)			1.8	0.0		0.8	0.0
NAO charges	Pt	-1.67	-1.13	-1.14	-1.35	-1.09	-1.08
	H	-0.39	-0.40	-0.41		-0.42	-0.40
	Ag _{ico} (av.)	0.59	0.36	0.36	0.29	0.34	0.33
	Ag _{cap} (av.)		0.70	0.70	0.70	0.65	0.66
Wiberg bond indices	Pt-H	0.292	0.196	0.197		0.195	0.197
	Ag-H (av.)	0.086	0.101	0.103		0.101	0.098
	Pt-Ag (av.)	0.216	0.135	0.133	0.148	0.123	0.125
	Ag _{ico} -Ag _{ico} (av.)	0.086	0.082	0.082	0.042	0.081	0.082
	Ag _{cap} -Ag _{ico} (av.)		0.043	0.041	0.087	0.044	0.042

For table of content only

